Engineered Magnetic Shape Anisotropy in BiFeO₃–CoFe₂O₄ Self-Assembled Thin Films

Zhiguang Wang,[†,*] Yanxi Li,[†] Ravindranath Viswan,[†] Bolin Hu,[‡] Vincent G. Harris,[‡] Jiefang Li,[†] and Dwight Viehland[†]

[†]Department of Materials Science and Engineering, Virginia Polytechnic Institute and State University, Blacksburg, Virginia 24061, United States and [‡]Department of Electrical and Computer Engineering, Northeastern University, Boston, Massachusetts 02115, United States

ABSTRACT We report growth of various phase architectures of self-assembled BiFeO₃–CoFe₂O₄ (BFO–CFO) thin films on differently oriented SrTiO₃ (STO) substrates. CFO forms segregated square, stripe, and triangular nanopillars embedded in a coherent BFO matrix on (001)-, (110)-, and (111)-oriented STO substrates, respectively. Nanostructures with an aspect ratio of up to 5:1 with a prominent magnetic anisotropy were obtained on both (001) and (110) STO along out-of-plane and in-plane directions. Magnetic easy axis rotation from in-plane to out-of-plane directions was realized through aspect ratio control. An intractable in-plane anisotropy was fixed in CFO on (111) STO due to the triangular shape of the ferromagnetic phase nanopillars. These studies established a detailed relationship of magnetic anisotropy with specific shape and dimensions of ordered magnetic arrays. The results suggest a way to effectively control the magnetic anisotropy in patterned ferromagnetic oxide arrays with tunable shape, aspect ratio, and elastic strain conditions of the nanostructures.
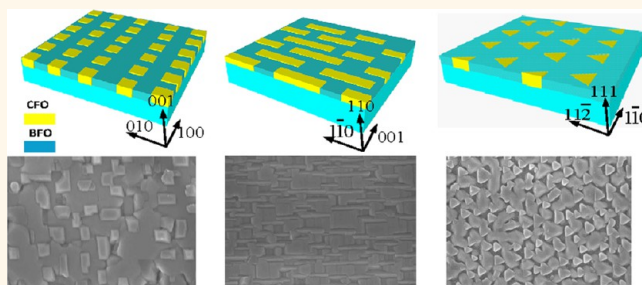
KEYWORDS: BiFeO₃–CoFe₂O₄ · self-assembled thin film · magnetic shape anisotropy

Magnetic oxides have been intensively investigated for their magnetic, magnetoresistive, magnetostrictive, and magneto-optical properties.[1,2] CoFe₂O₄ (CFO) is an ideal candidate for multiferroic and spintronic devices due to its large magnetocrystalline anisotropy and magnetostriction, chemical stability, and unique nonlinear spin-wave properties.[3,4] A strong spin–orbit coupling results in a large magnetostriction of $\lambda = -350 \times 10^{-6}$ and a large magnetization of 360 emu/cm³, which promises a large magnetic shape anisotropy.[5] Thus, the magnetic behavior of CFO is strongly dependent on nanostructure shape, size, domain configuration, and strain conditions.[6–8] Magnetic nanostructures with a magnetic anisotropy have usually only two stable orientations antiparallel to each other, separated by an energy barrier. The stable orientations define the nanoparticle's so-called "easy axis". The Néel relaxation time is an exponential function of the grain volume,[9] thus in sufficiently small single domain nanoparticles, the magnetization can randomly flip direction under the influence of temperature (i.e., superparamagnetism). Shape anisotropy is a phenomenon associated with the zeroth spatial order of the magnetization field and is predicted to produce the largest coercive forces.[10] Therefore, shape anisotropy has an advantage in aligning the magnetic easy axis of nanoparticles with respect to the surface when assembled into high-quality 2D and 3D arrays.[11]

The magnetic properties of nanostructures are strongly dependent on their morphologies (size, shape, core–shell relationship, particle arrangement in the matrix, etc.).[12] Even small deviations from spherical shapes can significantly alter the coercivity.[13] Therefore, patterned magnetic nanostructures have attracted much research interest due to their potential application in high-density magnetic recording media. Thus far, the attempts to fabricate ordered magnetic oxides have been focused mainly on three
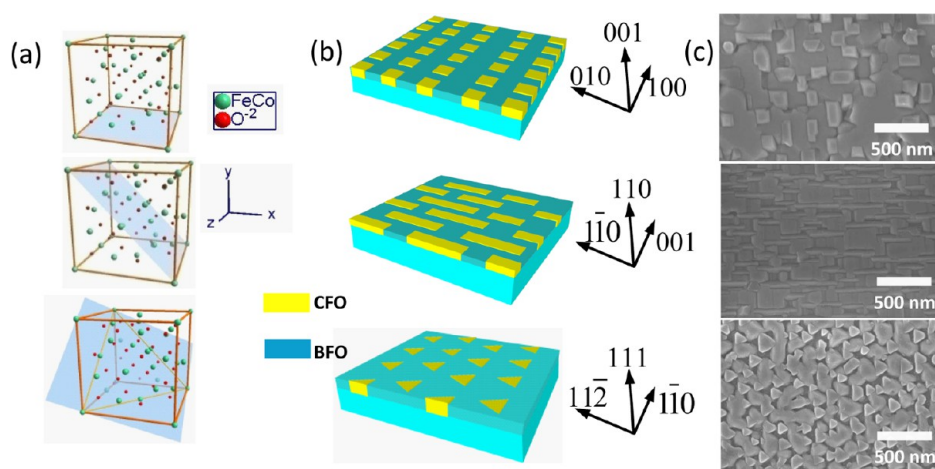
Figure 1. (a) Crystal structure of converse spinel CFO with the (001), (110) and (111) planes entitle. (b) Schematic of phase architectures for differently oriented BFO−CFO thin films on STO substrates. (c) SEM of BFO−CFO with square, stripe, and triangular CFO features.

means: (i) a top-down lithography;[14] (ii) a template-assisted deposition;[3] and (iii) a precipitation of immiscible phases that would form specific patterns through spontaneous phase separation.[4] With regards to the lithographic technique, the minimal size of patterned oxide magnets is confined by the refractory and chemical inertness of CFO compared with traditional silicon substrates. Nanoporous anodic aluminum oxide (AAO) membranes as stencil masks have been employed to fabricate CFO nanodot arrays.[3] However, it is difficult to obtain CFO nanostructures with a high aspect ratio using these methods, due to the growth mechanism and the subsequent lift-off from the membrane. Moreover, the shape of the dot arrays is confined by the AAO holes. On the other hand, both the aspect ratio and the specific shape of the nanostructures have been controlled in self-assembled multifunctional nanostructures,[5] examples include (i) a lateral size tuning by thermodynamic growth at different deposition temperatures, (ii) a height/length ratio control by deposition time, and (iii) a nanoarray shape tailoring by orientation of the substrate.

Magnetic anisotropy is a key factor in the development of high-density memory devices. Superparamagnetic effects can be surpressed and a stable magnetization promoted in ultrasmall nanostructures via magnetic anisotropy. In bulk CFO materials, the magnetocrystalline anisotropy occurs due to a spin−oribit coupling, whereas, in nanostructured CFO, the magnetic anisotropy is dominated mainly by the nanostructure shape, elasticity, and other interfacial effects.[14] It is well-known that perovskite BFO and spinel CFO spontaneously segregate due to an immiscibility when grown on SrTiO$_3$ (STO) substrates.[15] BFO is ferroelectric with a rhombohedral R3c structure that can be described as pseudocubic (a = 3.96 Å), whereas CFO is a ferromagnetic spinel with a cubic Fm3m structure (a = 8.39 Å) having a magnetic easy axis along the ⟨100⟩

direction.[16,17] STO has a cubic structure with a lattice parameter of a_c = 3.91 Å. BFO−CFO self-assembled heterostructures have vertically aligned interfaces which induce a compressive strain on the CFO nanoarrays due to the crystal lattice mismatch between the BFO and CFO phases (8.39 > 3.96 × 2). Perpendicular magnetic anisotropy has been reported and attributed to the compressive strain at the BFO−CFO interface. However, TEM analysis of a similar BiFeO$_3$−NiFe$_2$O$_4$ system has shown a fully relaxed interface with a large interfacial lattice mismatch. Lattice constant measurements in the out-of-plane direction revealed a strain of less than 0.1%, whereas the lattice mismatch of BFO and CFO was 5.6%. In addition, BFO, CFO, and STO have different thermal expansion coefficients, thus an internal strain will be introduced during the high-temperature deposition process that makes the strain condition more complex in the BFO−CFO two-phase system. In this case, it is difficult to determine the strain of the CFO only by the lattice mismatch with the surrounding phase. CFO has a large saturation magnetization (M_s = 360 emu/cm^3) which promises a large shape anisotropy energy of $K_{shape} = 2\pi N M_s^2$, where N is the demagnetization factor that is related to the shape and aspect ratio of the nanostructures.[18] As the CFO particle size is decreased to the micrometer level, the shape anisotropy energy will be much more dominant. Accordingly, an effective means to control the magnetic properties is by tuning of the shape and aspect ratio of the CFO nanoarrays. Here, the BFO−CFO system was used to grow CFO nanoarrays with regular shape and aspect ratios in order to study the magnetic shape anisotropy properties.

RESULTS AND DISCUSSION

Figure 1 shows the phase architectures of BFO−CFO grown on differently oriented STO substrates. CFO has a converse spinel crystal structure, whereas BFO has a
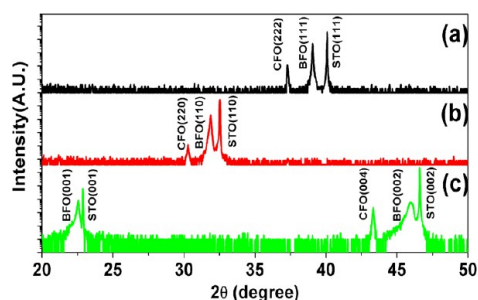
Figure 2. (a–c) Out-of-plane X-ray diffraction line scan of BFO–CFO on (111), (110), and (100) STO substrates.

rhombohedrally distorted perovskite one. The large crystal lattice mismatch (7.4%) between CFO and STO induces a big surface energy difference, and a lack of "wetting" on STO drives CFO to form nanopillars embedded in a coherent BFO matrix which has a close lattice constant to that of STO. Scanning electron microscopy (SEM) images in panel c reveal feature morphologies of square, stripe, and triangular nano-structured CFO on (001)-, (110)-, and (111)-oriented STO substrates, respectively.

We then examined the out-of-plane crystallographic orientation of the BFO–CFO composite thin films on differently oriented STO substrate by XRD θ–2θ scans, as shown in Figure 2. Diffraction peaks of atomic planes in accordance with the orientation of the STO substrate were observed. This indicates an epitaxial growth mechanism and evidencing phase separation.

Figure 3 summarizes how the magnetic properties of BFO–CFO on (001) STO changed with dimensions. A magnetic force microscopy (MFM) probe was mag-netized in the spin-up direction. The black and white areas in the MFM images demonstrate spin-up and spin-down magnetic domains, indicating a perpendi-cular push–pull magnetic moment coupling between the probe and the CFO nanopillars. First, we studied the magnetic response in a BFO–CFO film with a thickness of 500 nm, where the diameter of the CFO nanopillars was 100 nm, that is, a height to diameter ratio of $R \approx 5$. The thin film thickness was determined by direct measurement of the cross-sectional SEM images. We have examined the lateral size of the CFO nanopillars in BFO–CFO thin films by cutting the sample with a focus ion beam, and a uniform width could be observed.[19] Therefore, the aspect ratio can be calculated by dividing the thickness by the lateral size of the CFO features. The shape anisotropy energy density of a CFO cylinder with an aspect ratio of 5:1 and a demagnetization factor of $N_z = 0.04$ can be esti-mated as $E_{shape} = 2\pi(N_x - N_z)M_s^2 = 4.2 \times 10^5$ erg/cm^3, where $N_x = (1 - N_z)/2$.[20,21] The shape anisotropy field was calculated to be $H_{shape} = 2E_{shape}/M_s = 1.9$ kOe. Accordingly, the CFO nanopillars should have a pro-nounced out-of-plane magnetic easy axis. Black and white square areas of similar proportion can be seen in

the MFM image of Figure 3a, indicating a near random distribution of up and down magnetizations for the as-prepared BFO–CFO. Then, a perpendicular 5 kOe magnetic field was applied along both up and down directions. Changes in the MFM image were used to study the remnant magnetization in each CFO nano-pillar. Figure 3b shows a MFM image of CFO in the down magnetized state. Uniform white rectangles of ~100 nm size show that the CFO nanopillars are predominantly in a similar single domain state. A near complete switching of the magnetization direction (from black to white) was observed in the square CFO areas under −5 kOe, as can be seen in the MFM images of Figure 3c.

To confirm that the shape anisotropy is more sig-nificant than other effects in the BFO–CFO with large aspect ratios, we measured the M–H loops for different rotation angle (θ) from in-plane to out-of-plane direc-tions. For CFO square pillars with a finite length, the easy axis should be in the longest dimension direction due to shape anisotropy, as illustrated by the arrow in Figure 3d. BFO–CFO films with thicknesses of 500 and 300 nm were selected, where the aspect ratio varied from $R = 5:1$ to 3:1. Figure 3e,f shows the evolution of the M–H loops as the measurement angle was rotated from in-plane to out-of-plane directions for CFO nano-pillars with aspect ratios of 5:1 and 3:1, respectively. A large magnetic perpendicular shape anisotropy can be seen in the 500 nm BFO–CFO layer, where the remnant magnetization (M_r) in the out-of-plane direc-tion was four times larger than that in-plane. The coercive field in the out-of-plane direction reached $H_c = 2.5$ kOe, which was almost three times larger than that in-plane (0.9 kOe). The magnetic field was not sufficiently high to saturate the magnetization, so the coercive field difference $H_{diff} = 2.5−0.9 = 1.6$ kOe was smaller than the calculated anisotropy field (1.9 kOe). The M–H loops for BFO–CFO with a smaller R (3:1) showed a weaker magnetic anisotropy. The remnant magnetizations (after normalization) were 0.28 and 0.11 in the OP and IP directions, respectively. The coercive fields were also much smaller: 1.5 and 0.608 kOe for OP and IP directions, respectively. It is well-known that the coercive field for single domain magnetic nanostructure decreases rapidly as the size is decreased.[22−24] Therefore, the decrease of the mag-netic anisotropy and the coercive field when R was changed from 5:1 to 3:1 can be attributed to size and shape anisotropy effects instead of a strain anisotropy one, as the strain conditions should be identical for the BFO–CFO system.

Figure 3g shows the remnant magnetization as a function of the IP to OP rotation angle. For a square shape with a specific aspect ratio R, the longest dis-tance should be along the direction indicated by an arrow in Figure 3d, where $\theta = \arctan(R)$. For a large R, the value of θ was very close to 90°: thus, the 500 nm
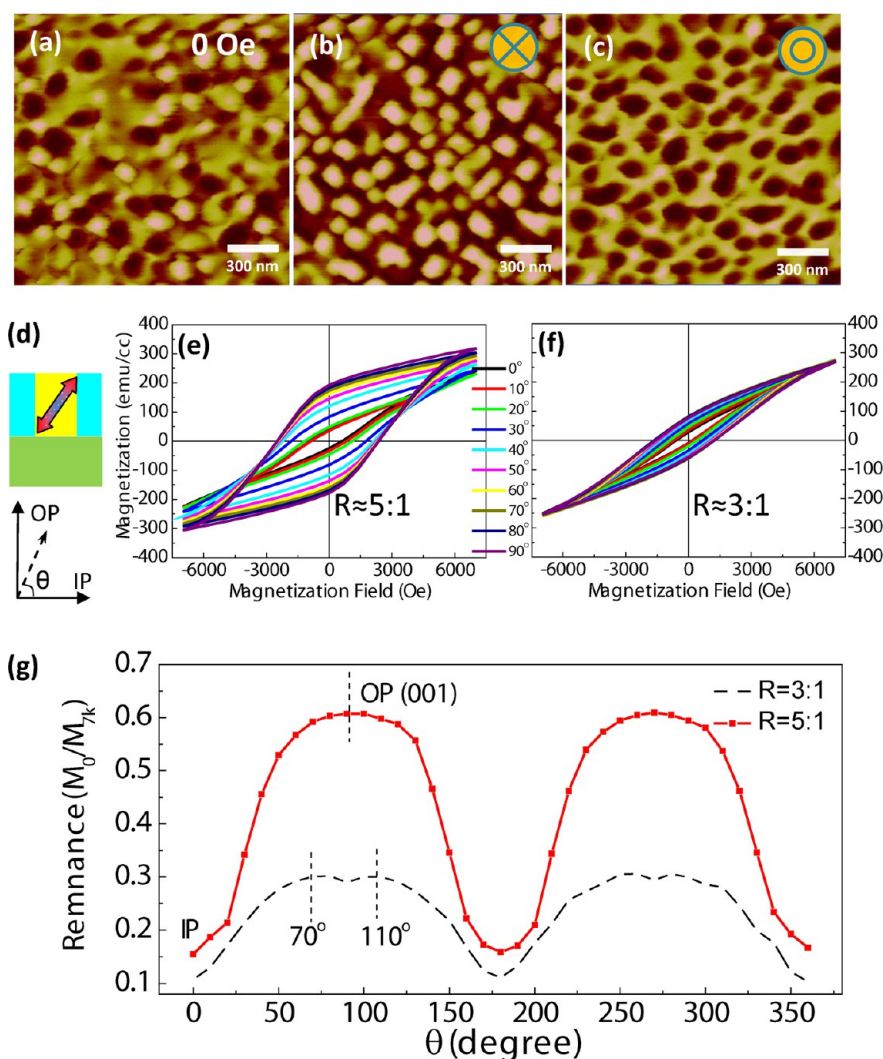
Figure 3. (a–c) MFM images of single domain CFO nanopillars after applying different magnetic fields. (d–f) M–H loops for different measurement angles of CFO nanopillars with different aspect ratios. (g) Remnant magnetization as a function of in-plane to out-of-plane rotation angle.

BFO–CFO thin film had the highest remnance value of 0.6 along the OP direction. For a 300 nm BFO–CFO thin film with R = 3:1, the easy axis angle is θ = arctan(3) = 71 or 109°. Accordingly, the largest remnance values observed in the M–H loops occurred at θ = 70 and 110°. These results unambiguously demonstrate that the shape anisotropy is a predominant factor for BFO–CFO self-assembled nanostructures on (001) STO, where the easy axis direction can be rotated by tuning of the aspect ratio of the CFO nanopillars.

The CFO phase has a large saturation magnetization, and thus the magnetic anisotropy should be sensitive to the strain conditions of the CFO nanostructure. We studied the strain relaxation as a function of the film thickness, as given in Figure 4a. The 200 nm CFO thin films on STO showed a (400) peak at 43.166°, which was quite stable as the thickness changed. This corresponds to a crystal lattice parameter a_c = 8.3815 Å, which is slightly smaller than that of CFO bulk.

In BFO–CFO self-assembled thin films, CFO is confined by a compressive strain from the BFO matrix. This strain will relax as the thin film thickness increases. As the BFO–CFO thickness increased from 200 to 900 nm, the CFO diffraction peaks shifted from 43.215 to 43.185°, indicating a strain relaxation from 0.079 to 0.03%. The strain anisotropy energy density was then compared with the shape-induced ones for BFO–CFO films with different thicknesses, as given in Figure 4c. The strain-induced anisotropy energy was larger for BFO–CFO with small aspect ratios. However, as the film thickness increased, the shape anisotropy will become more and more important. We also measured the magnetic coercive field as a function of the thickness, as shown in Figure 4c. With increasing thickness, the strain effect from the BFO matrix was relaxed, thus the value of H_c should decrease if the strain effect is the only source of the magnetic anisotropy in BFO–CFO. However, H_c increased from 1.2 to 2.53 and then to 3.4 kOe as the BFO–CFO thickness increased from 300 to 500 and
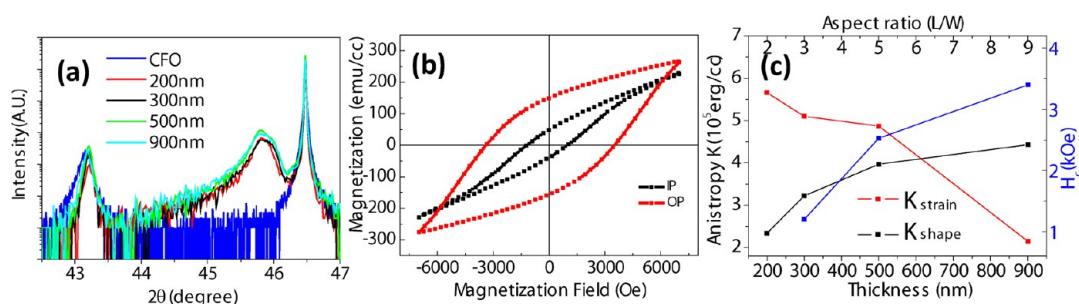
Figure 4. (a) X-ray line scan of pure CFO and BFO–CFO thin films with different thickness. (b) M–H loops for 900 nm BFO–CFO in IP and OP directions. (c) Comparison of strain- and shape-induced magnetic anisotropy energy density (K) and magnetic coercive field (H_c) as a function of BFO–CFO thickness.
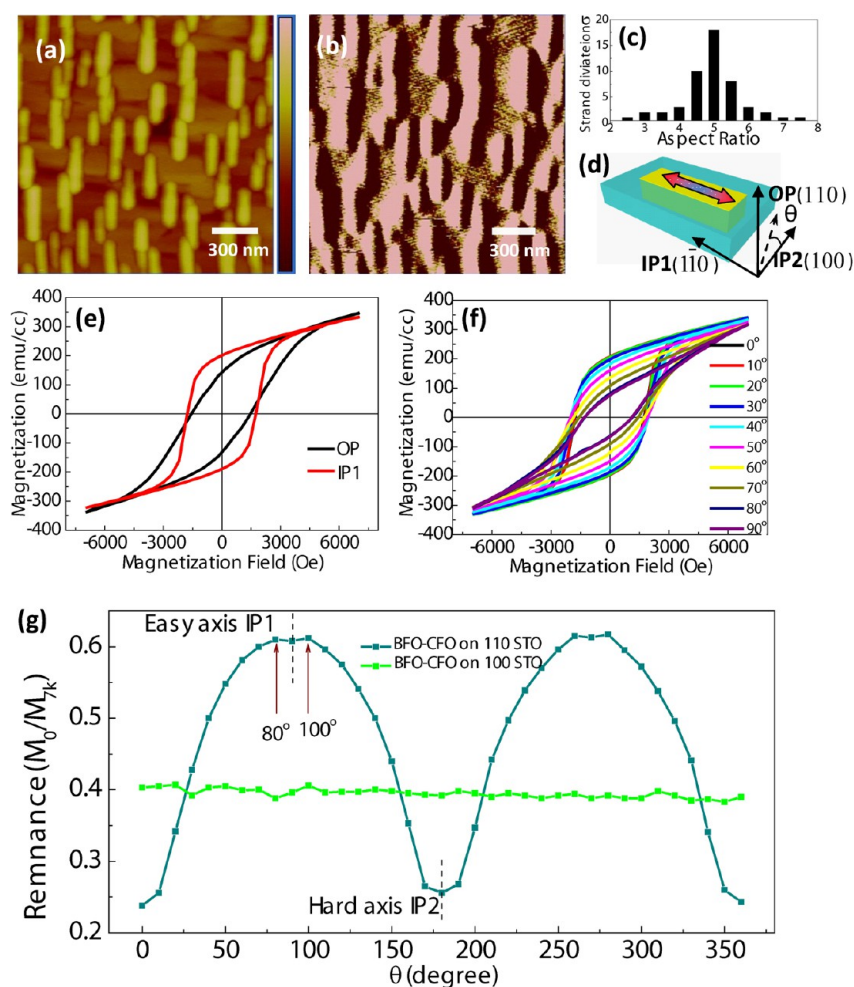

Figure 5. (a,b) AFM and MFM images of BFO–CFO on (110) STO (AFM error bar: 50 nm). (c) Schematic of magnetic easy axis in the in-plane direction. (d) M–H loops of (110) BFO–CFO in IP and OP directions. (e) M–H loops of BFO–CFO on (110) STO with different in-plane directions. (f) Remnant magnetization as a function of in-plane rotation angle θ for BFO–CFO on (100) and (110) STO.

then to 900 nm due to the existence of shape anisotropy effect.

Figure 5 summarizes the magnetic properties of BFO–CFO on (110) STO substrates, where the morphological features were aligned along the in-plane direction. The deposition temperature was set to be 700 °C for the requirement of well-separated phase distribution which is related to the growth thermal dynamics.

Both growth rate and deposition temperature can affect the feature size of CFO nanostripes: faster growth rate and higher deposition temperature will produce CFO nanostripes with larger width and length values. Detailed CFO nanostructure dimension control can be found in our previous results.[25] The CFO phase formed as nanostripes with $R \approx$ 5:1 that were oriented in the in-plane direction, with lengths of ~300 nm and widths of
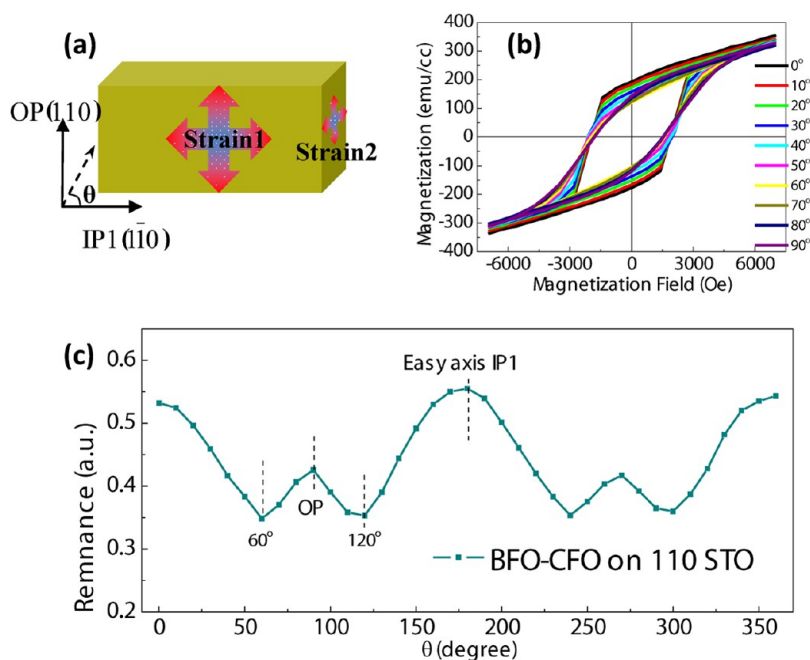
Figure 6. (a) Schematic of two different strain effects in the BFO−CFO interfaces along different directions. (b) $M−H$ loops of BFO−CFO with different in-plane rotation angles from IP1 direction. (c) Magnetic remnance as a function of in-plane rotation angle θ.

~60 nm. Panel a gives an atomic force microscopy (AFM) topography which shows that the CFO nanostripes were slightly higher than the BFO matrix, and panel b is a corresponding MFM image where a strong magnetic response was evident in the CFO phase but not in the BFO matrix. The dimensions of CFO nanostripes were not uniform, and a stand deviation on the aspect ratio is shown in panel c. The CFO phase has a large magnetocrystalline anisotropy of $K_1 = 2 \times 10^6$ erg/cm^3: thus, the crystalline anisotropy energy difference between the $\langle 001 \rangle$ and $\langle 110 \rangle$ directions is $\Delta E = K_0 - (K_0 + K_1/4) = 5 \times 10^5$ erg/cm^3,[21] which is close to the shape anisotropy energy for a nanostructure with an aspect of $R = 5:1$. However, it has been reported that the effective magnetocrystalline anisotropy energy (K_{eff}) is strongly dependent on the size of the magnetic nanostructures: K_{eff} will decrease as the particle size decreases.[26−28] The $M−H$ loops for BFO−CFO on (001) STO substrate exhibited similar ferromagnetic behavior when referenced to their in-plane $\langle 001 \rangle$ and $\langle 1\bar{1}0 \rangle$ directions. The crystal lattice mismatch between CFO and STO is 7.7%, while that of CFO and BFO is 6.06%. The large crystal lattice mismatch will induce excessive misfits in the longitudinal and perpendicular interfaces. Lower coordinated atoms at the surface will then play a more significant role. Therefore, the magnetocrystalline anisotropy is further decreased. Accordingly, an easy axis along the length can be expected for BFO−CFO on (110) STO, that is, the IP1 direction in panel d, where IP1 denotes the long axis $\langle 1\bar{1}0 \rangle$ of CFO nanostripes and IP2 the short axis of $\langle 001 \rangle$. The $M−H$ loops for the BFO−CFO epitaxial layers in both IP and

OP directions are shown in panel e. The thickness of the sample was 200 nm, thus the aspect ratio between IP1 and OP was 3:2. IP1 is the easy axis with a much larger M_r, which also had a larger H_c compared with the OP direction. The value of M_r was then measured as a function of the in-plane rotation angle θ, as shown in panel g. A sine-like wave function for M_r can be seen with a large M_r in the IP1 direction (0.79) and a small M_r along IP2 (0.33). Again, the largest M_r was observed in the directions around OP (80 and 100°) due to the limited R value. These results demonstrate a strong anisotropy for BFO−CFO layers. This phenomenon offers an effective method to solve the problem of the superparamagnetic limit, where the existence of a strong easy axis may provide an enhanced tolerance to track misregistration and side-writing for longitudinal recording.[29] Although the sizes of the CFO nanostructures in BFO−CFO self-assembled thin films (>100 nm) are far from the superparamagnetic limit (<10 nm),[30] the conclusions about BFO−CFO can be applied to all other artificial magnetic nanoarrays, such as self-assembled BTO−CFO, where the CFO feature size can reach around 20 nm.[4]

For BFO−CFO on (110) STO, there are two different interfaces along the IP1 and IP2 directions, respectively, as shown in Figure 6a. The interface along the IP1 direction is 5 times larger than that along IP2 for a CFO nanostripe with an aspect ratio of 5:1. A biaxial strain should result in a similar magnetic strain anisotropy in in-plane and out-of-plane directions for each BFO−CFO interface. However, in the out-of-plane
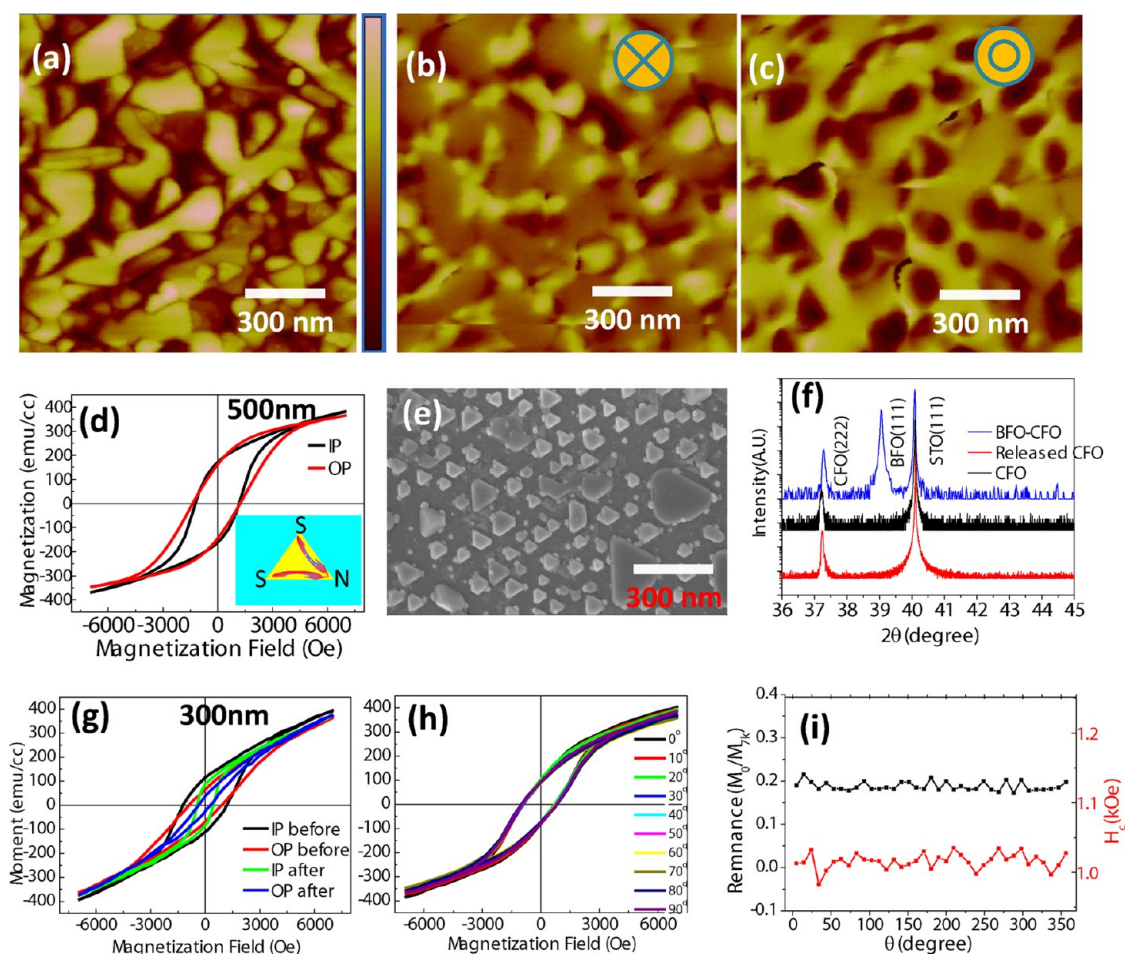
Figure 7. (a−c) AFM and MFM images of 500 nm BFO−CFO films on (111) STO with different magnetic configurations (AFM error bar: 125 nm). (d) M−H loops for 500 nm BFO−CFO on (111) STO and a schematic of demagnetization field (inset). (e) Top-view SEM of released CFO prism arrays. (f) Comparison of XRD results for BFO−CFO, released CFO, and pure CFO thin films. (g) M−H loops of BFO−CFO and released CFO. (h) M−H loops for BFO−CFO with different in-plane rotation angle. (i) Magnetization remnance and H_c as a function of in-plane rotation angle θ.

direction, the effect of strain 1 and strain 2 can be added together as they both act along the same direction, whereas the strain effects act separately along the IP1 and IP2 directions. Thus, the strain along the three different directions can be roughly estimated to be $S_{op}:S_{ip1}:S_{ip2}$ = 6:5:1. The CFO crystal structures along ($\bar{1}$10) and (110) directions are identical, thus there is no magnetocrystalline anisotropy between IP1 and OP. We measured the M−H loops for 200 nm BFO−CFO thin film with different IP1 to OP rotation angles, as shown in Figure 6b,c. IP1 is the length direction of the CFO nanostripes; thus, it is the magnetic easy axis, which had a magnetic remnance of 0.55. The OP direction is expected to be the magnetic hard axis as a result of the magnetic shape anisotropy. However, smaller remnance values (∼0.35) were found for θ = 60 and 120° relative to the value (0.43) at θ = 90° along the OP direction: this is due to the existence of a compressive strain along the OP direction, which induces an out-of-plane magnetic anisotropy. The total magnetic anisotropy is the competing effect of the IP1 shape anisotropy and the OP strain anisotropy, where

TABLE 1. Comparison of Coercive Field (H_c) and Remnant Magnetization (M_r) for BFO−CFO and Released CFO Nanoarray Structures in Both In-Plane (ip) and Out-of-Plane (op) Directions

structure	$H_{c\text{-ip}}$(Oe)	$H_{c\text{-op}}$(Oe)	$H_{c\text{-ip}}/H_{c\text{-op}}$	$M_{r\text{-ip}}$(emu/cc)	$M_{r\text{-op}}$(emu/cc)	$M_{r\text{-ip}}/M_{r\text{-op}}$
BFO−CFO	1235	889	1.39	115	66	1.74
released CFO	450	320	1.40	89	38	2.34

shape anisotropy is more significant, resulting in a uniaxial in-plane magnetic easy axis along the IP1 direction.

Figure 7 shows the phase architecture and magnetic response of a BFO−CFO film on (111) STO. Although it has been reported that CFO has a smaller surface energy mismatch with STO compared with the BFO phase,[5] we found that CFO formed as segregated triangular cylinders embedded in a coherent BFO matrix. A BFO−CFO thin film with a thickness of 500 nm was selected due to a comparatively large out-of-plane magnetic anisotropy (compared with thinner films) which favors MFM measurements.

TABLE 2. Phase Architecture, Morphology, and Magnetic Anisotropy of BFO—CFO Self-Assembled Thin Films Grown on Differently Oriented STO Substrates

substrate orientation	CFO shape	lateral size (nm)	thickness (nm)	shape anisotropy	strain anisotropy	crystalline anisotropy	total anisotropy
100	square	100	300, 500, 900	OP	OP	N/A	OP (uniaxial)
110	stripe	60 (W), 300 (L)	200	IP	OP	N/A	IP (uniaxial)
111	triangle	100	300, 500	IP	OP	N/A	IP (biaxial)

Panels a—c show AFM and MFM images of BFO—CFO having different magnetization states. Black triangular areas can clearly be seen in panel b, indicating a spin-up state in the CFO pillars under −5 kOe, whereas the white ones in panel c indicate a switching to spin-down under 5 kOe. The M—H loop of the 500 nm BFO—CFO on (111) STO is given in panel d, where it can be seen that M_r in the in-plane direction is still larger than that out-of-plane. This intractable in-plane easy axis can be attributed to the shape edge of the triangular CFO pillars. The magnetic pole density is strongest in the tip area of the triangles, resulting in a large demagnetization field, as illustrated in the inset schematic in panel d. In this case, the demagnetization factor N_{ip} is much smaller compared with that of an elliptical one. This will then pin the easy axis along the in-plane direction. To confirm this phase architecture, we annealed a BFO—CFO film with thickness of 300 nm at 860 °C for 3 h to evaporate bismuth and decompose the BFO perovskite phase. Detailed procedure can be found in our previous work about release of BFO—CFO on (100) STO substrates.[31] We then used acid to etch the remaining iron oxide reduced from BFO. Distinct CFO triangular pillars can be seen in top-view SEM image, as shown in panel e. The release effect was also confirmed by the XRD results. In panel f of the figure, BFO—CFO, released CFO, and pure CFO diffraction peaks can clearly be seen. A compressive strain value of 0.079% in the CFO phase of the BFO—CFO layer was estimated by comparing with pure CFO thin films on (111) STO. After annealing and etching of the BFO matrix, the (111) diffraction peak from BFO disappeared, whereas the CFO (222) peak remained but was shifted from $2\theta =$ 37.28 to 37.22°; this is due to the release of compressive strain from the BFO matrix. Then, the M—H loops for 300 nm BFO—CFO were compared for the states before and after the releasing procedure, as shown in panel g. Despite the large strain along the out-of-plane direction, the BFO—CFO film still exhibited an in-plane magnetic anisotropy with a larger remnant magnetization and a larger H_c along the in-plane direction compared to that along the out-of-plane one. For the released CFO nanoarrays, the value of H_c was significantly decreased due to the release of the compressive strain and to the fact that the in-plane magnetic anisotropy becomes much more significant. Detailed magnetic response changes are given in Table 1. Also, the M—H loops for 300 nm BFO—CFO thin film on (111)

STO with different in-plane rotation angles, as shown in Figure 7h,i. No significant change could be found in either H_c or magnetic remnance values as a function of the in-plane rotation angle θ.

Table 2 summarizes the phase distribution, morphology, and magnetic anisotropy for BFO—CFO thin films grown on (100), (110), and (111) STO substrates. Dramatic difference can be found for BFO—CFO with different shapes, and the total magnetic anisotropy is the cooperating effect of shape and strain anisotropy. In (100)-oriented BFO—CFO (thickness >100 nm), magnetic shape anisotropy and strain anisotropy are all in the OP direction, thus the easy axis is along the OP direction. For (110)-oriented BFO—CFO, the magnetic shape anisotropy lies along the IP1($1\bar{1}0$) direction, whereas the strain anisotropy is along OP. The competing effect results in an easy axis in the IP1 direction and a hard axis that is 30° from the OP direction. In (111)-oriented BFO—CFO, the sharp edge of the CFO prism results in a large IP magnetic anisotropy, while the strain anisotropy is along the OP direction. The easy axis is in the OP direction. No obvious magnetocrysalline anisotropy has been found due to the small size of CFO nanostructures with large surface-to-volume ratio.

CONCLUSIONS

We have deposited BFO—CFO self-assembled thin films on three differently oriented STO substrates with different phase architectures. CFO forms square nanopillars on (001) STO with a lateral size of around 100 nm, where the aspect ratio could be manipulated by the height of the nanopillars. Complete magnetization switching in each CFO nanopillar was observed in the MFM images. Nanostriped CFO was then deposited on (110) STO substrates with an in-plane aspect ratio of $R =$ 5:1. The hard axis was around the OP direction due to the competing of magnetic shape and strain effects. An easy axis was found along the length direction due to a stronger magnetic shape anisotropy compared with the strain one. CFO had a triangular pillar morphology when deposited on (111) STO. An intractable in-plane easy axis indicated a strong demagnetization field induced by a large magnetization gradient in each triangular pillar along the in-plane direction. These results illustrate an important relationship between magnetic properties with specific shapes and aspect ratios for BFO—CFO self-assembled heterostructures.

Development of ferromagnetic artificial patterns of nanometer size with controllable magnetic anisotropy may offer application in high-density perpendicular storage.

EXPERIMENTAL METHODS

Fabrication Procedures. BFO—CFO self-assembled nanostructures were prepared by pulsed laser deposition using a 248 nm KrF laser and a composite target of composition 65 atom % BFO and 35 atom % CFO. The (001)-, (110)-, and (111)-oriented STO substrates were used for the growth of BFO—CFO with different phase architectures. Growth was carried out at 700 °C in an oxygen atmosphere (150 mTorr) with a laser energy density of 3 J/cm^2 at 10 Hz. The distance between the target and substrates is 6 cm. Etching of the annealed BFO—CFO was performed in dilute HCl (50%, v/v) for 1 h at room temperature.

Characterization of Structure and Properties. The phase distribution and thickness of BFO—CFO thin films were characterized by a LEO (Zeiss) 1550 field-emission SEM to obtain top-view images. The crystal lattice and thin film orientation were analyzed by a Philips X'pert high-resolution X-ray diffractometer designed for single-crystalline samples. Topography and magnetic properties were studied by a Veeco SPI 3100 working in AFM and MFM modes, respectively. MFM images was obtained with a magnetic tip working at lift mode with a lift height of 20 nm. Magnetic hysteresis loops were measured using a Lakeshore 7300 series vibrating sample magnetometer system at room temperature.

Conflict of Interest: The authors declare no competing financial interest.

REFERENCES AND NOTES

1. Ramesh, R.; Spaldin, N. A. Multiferroics: Progress and Prospects in Thin Films. *Nat. Mater.* **2007**, *6*, 21–29.
2. Eerenstein, W.; Mathur, N. D.; Scott, J. F. Multiferroic and Magnetoelectric Materials. *Nature* **2000**, *442*, 759–765.
3. Gao, X. S.; Liu, L.; Lee, W.; Birajdar, B I.; Ziese, M.; Alexe, M.; Hesse, D. High-Density Periodically Ordered Magnetic Cobalt Ferrite Nanodot Arrays by Template-Assisted Pulsed Laser Deposition. *Adv. Funct. Mater.* **2009**, *19*, 3450–3455.
4. Zheng, H.; Wang, J.; Lofland, S. E.; Ma, Z.; Mohaddes-Ardabili, L.; Zhao, T.; Salamanca-Riba, L.; Shinde, S. R.; Ogale, S. B.; *et al.* Multiferroic BaTiO$_3$—CoFe$_2$O$_4$ Nanostructures. *Science* **2004**, *303*, 661–663.
5. Zheng, H. M.; Zhan, Q.; Zavaliche, F.; Sherburne, M.; Straub, F.; Cruz, M P.; Chen, L. Q.; Dahmen, U.; Ramesh, R. Controlling Self-Assembled Perovskite-Spinel Nanostructures. *Nano Lett.* **2006**, *6*, 1401–1407.
6. Eerenstein, W.; Wiora, M.; Prieto, J. L.; Scott, J. F.; Mathur, N. D. Giant Sharp and Persistent Converse Magnetoelectric Effects in Multiferroic Epitaxial Heterostructures. *Nat. Mater.* **2007**, *6*, 348–351.
7. Zavaliche, F.; Zheng, H.; Mohaddes-Ardabili, L.; Yang, S. Y.; Zhan, Q.; Shafer, P.; Reilly, E.; Chopdekar, R.; Jia, Y.; Wright, P.; *et al.* Electric Field-Induced Magnetization Switching in Epitaxial Columnar Nanostructures. *Nano Lett.* **2005**, *5*, 1793–1796.
8. Liao, S. C.; Tsai, P. Y.; Liang, C. W.; Liu, H. J.; Yang, J. C.; Lin, S. J.; Lai, C. H.; Chu, Y. H. Misorientation Control and Functionality Design of Nanopillars in Self-Assembled Perovskite—Spinel Heteroepitaxial Nanostructures. *ACS Nano* **2011**, *5*, 4118–4122.
9. Fannin, P. C.; Charles, S. W. On the Calculation of the Neel Relaxation Time in Uniaxial Single-Domain Ferromagnetic Particles. *J. Phys. D: Appl. Phys.* **1994**, *27*, 185–188.
10. Leslie-Pelecky, D. L.; Rieke, R. D. Magnetic Properties of Nanostructured Materials. *Chem. Mater.* **1996**, *8*, 1770–1783.
11. Cowburn, R. P. Property Variation with Shape in Magnetic Nanoelements. *J. Phys. D: Appl. Phys.* **2000**, *33*, R1–R16.
12. Gubin, S. P.; Koksharov, Y. A.; Khomutov, G. B.; Yurkov, G. Y. Magnetic Nanoparticles: Preparation, Structure and Properties. *Russ. Chem. Rev.* **2005**, *74*, 489–520.
13. Srikala, D.; Singh, V. N.; Banerjee, A.; Mehta, B. R. Effect of Induced Shape Anisotropy on Magnetic Properties of Ferromagnetic Cobalt Nanocubes. *J. Nanosci. Nanotechnol.* **2010**, *10*, 8088–8094.
14. Takamura, Y.; Chopdekar, R. V.; Scholl, A.; Doran, A.; Liddle, J. A.; Harteneck, B.; Suzuki, Y. Tuning Magnetic Domain Structure in Nanoscale La$_{0.7}$Sr$_{0.3}$MnO$_3$ Islands. *Nano Lett.* **2006**, *6*, 1287–1291.
15. Yan, L.; Yang, Y.; Wang, Z.; Xing, Z.; Li, J.; Viehland, D. Review of Magnetoelectric Perovskite—Spinel Self-Assembled Nano-Composite Thin Films. *J. Mater. Sci.* **2009**, *44*, 5080–5094.
16. Bozorth, R. M.; Tilden, E. F.; Williams, A. J. Anisotropy and Magnetostriction of Some Ferrites. *Phys. Rev.* **1955**, *99*, 1788–1798.
17. Dix, N.; Muralidharan, R.; Rebled, J. M.; Estrsdé, S.; Peiró, F.; Varela, M.; Fontcuberta, J.; Sánchez, F. Selectable Spontaneous Polarization Direction and Magnetic Anisotropy in BiFeO$_3$—CoFe$_2$O$_4$ Epitaxial Nanostructures. *ACS Nano* **2010**, *4*, 4955–4961.
18. Comes, R.; Khokhlov, M.; Liu, H.; Lu, J.; Wolf, S. A. Magnetic Anisotropy in Composite CoFe$_2$O$_4$—BiFeO$_3$ Ultrathin Films Grown by Pulsed-Electron Deposition. *J. Appl. Phys.* **2012**, *111*, 07D914.
19. Wang, Z.; Yang, Y.; Viswan, R.; Li, J.; Viehland, D. Giant Electric Field Controlled Magnetic Anisotropy in Epitaxial BiFeO$_3$—CoFe$_2$O$_4$ Thin Film Heterostructures on Single Crystal Pb(Mg$_{1/3}$Nb$_{2/3}$)$_{0.7}$Ti$_{0.3}$O$_3$ Substrate. *Appl. Phys. Lett.* **2007**, *99*, 043110.
20. Zheng, H.; Kreisel, J.; Chu, Y.; Ramesh, R.; Salamanca-Riba, L. Heteroepitaxially Enhanced Magnetic Anisotropy in BaTiO$_3$—CoFe$_2$O$_4$ Nanostructures. *Appl. Phys. Lett.* **2007**, *90*, 113113.
21. Cullity, B. D.; Graham, C. D. *Introduction to Magnetic Materials*, 2nd ed.; Wiley: Hoboken, NJ, 2009.
22. Jun, Y. W.; Huh, Y. M.; Choi, J. S.; Lee, J. H.; Song, H. T.; Kim, S.; Yoon, S.; Kim, K. S.; Shin, J. S.; Suh, J. S.; *et al.* Nanoscale Size Effect of Magnetic Nanocrystals and Their Utilization for Cancer Diagnosis *via* Magnetic Resonance Imaging. *J. Am. Chem. Soc.* **2005**, *127*, 5732–5733.
23. Park, J. I.; Kang, N. J.; Jun, Y. W.; Oh, S. J.; Ri, H. C.; Cheon, J. Superlattice and Magnetism Directed by the Size and Shape of Nanocrystals. *Chem. Phys. Chem.* **2002**, *6*, 543–547.
24. Fischer, R.; Schrefl, T.; Kronmüller, H.; Fidler, J. Grain-Size Dependence of Remanence and Coercive Field of Isotropic Nanocrystalline Composite Permanent Magnets. *J. Magn. Magn. Mater.* **1996**, *153*, 35–49.
25. Yan, L.; Bai, F.; Li, J.; Viehland, D. Nanobelt Structure in Perovskite—Spinel Composite Thin Films. *J. Am. Ceram. Soc.* **2009**, *91*, 17–21.
26. Herzer, G. Grain Size Dependence of Coercivity and Permeability in Nanocrystalline Ferromagnets. *IEEE Trans. Magn.* **1990**, *26*, 1397–1402.
27. Grössinger, R.; Dehlgren, M. Exchange Coupled Hard Magnetic Materials in Pulsed High Magnetic Field. *Physica B* **1998**, *246–247*, 213–219.
28. Kronmüller, H.; Fischer, R.; Seeger, M.; Zern, A. Micromagnetism and Microstructure of Hard Magnetic Materials. *J. Phys. D: Appl. Phys.* **1996**, *29*, 2274–2283.
29. White, R. L.; Newt, R. M. H.; Pease, R. F. W. Patterned Media: A Viable Route to 50 Gbit/in^2 and Up for Magnetic Recording? *IEEE Trans. Magn.* **1997**, *33*, 990–995.

30. Berkowitz, A. E.; Schuele, W. J. Magnetic Properties of Some Ferrite Micropowders. *J. Appl. Phys.* **1959**, S134.

31. Wang, Z.; Viswan, R.; Viswan, R.; Hu, B.; Li, J.; Viehland, D.; Harris, V. Tunable Magnetic Anisotropy of $CoFe_2O_4$ Nanopillar Arrays Released from $BiFeO_3$ Matrix. *Phys. Status Solidi (RRL)* **2012**, *2*, 92–94.